JACS
JOURNAL OF THE AMERICAN CHEMICAL SOCIETY
Article
pubs.acs.org/JACS

Crystal Structure and Optical Properties of the $[Ag_{62}S_{12}(SBu^t)_{32}]^{2+}$ Nanocluster with a Complete Face-Centered Cubic Kernel

Shan Jin,[†,∥] Shuxin Wang,[†,∥] Yongbo Song,[†] Meng Zhou,[‡] Juan Zhong,[§] Jun Zhang,[†] Andong Xia,[‡] Yong Pei,[§] Man Chen,[†] Peng Li,[†] and Manzhou Zhu*[,†]

[†]Department of Chemistry and Center for Atomic Engineering of Advanced Materials, Anhui University, Hefei, Anhui 230601, People's Republic of China

[‡]The State Key Laboratory of Molecular Reaction Dynamics, and Beijing National Laboratory for Molecular Sciences (BNLMS), Institute of Chemistry, Chinese Academy of Sciences, Beijing 100190, People's Republic of China

[§]Department of Chemistry, Key Laboratory of Environmentally Friendly Chemistry and Applications of Ministry of Education, Xiangtan University, Xiangtan, Hunan 411105, People's Republic of China

Supporting Information

ABSTRACT: The crystal structure of the $[Ag_{62}S_{12}(SBu^t)_{32}]^{2+}$ nanocluster (denoted as **NC-I**) has been successfully determined, and it shows a complete face-centered-cubic (FCC) Ag_{14} core structure with a $Ag_{48}(SBu^t)_{32}$ shell configuration interconnected by 12 sulfide ions, which is similar to the $[Ag_{62}S_{13}(SBu^t)_{32}]^{4+}$ structure (denoted as **NC-II** for short) reported by Wang. Interestingly, **NC-I** exhibits prominent differences in the optical properties in comparison with the case of the **NC-II** nanocluster. We employed femtosecond transient absorption spectroscopy to further identify the differences between the two nanoclusters. The results show that the quenching of photoluminescence in **NC-I** in comparison to that of **NC-II** is caused by the free valence electrons, which dramatically change the ligand to metal charge transfer (LMCT, S 3p → Ag 5s). To get further insight into these, we carried out time-dependent density functional theory (TDDFT) calculations on the electronic structure and optical absorption spectra of **NC-I** and **NC-II**. These findings offer a new insight into the structure and property evolution of silver cluster materials.

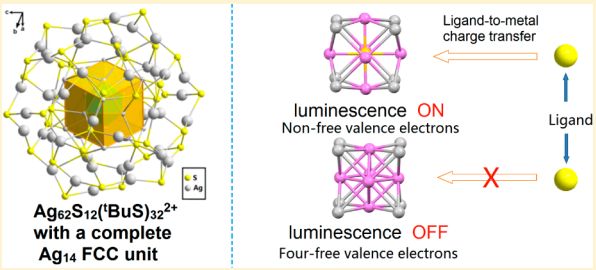

INTRODUCTION

Atomically precise metal nanoclusters have recently emerged as a new frontier in nanoscience research, owing to their novel properties and promising applications in various fields, such as biomedicine,[1] chemical sensing,[2] bioassays,[3] biolabeling,[4] magnetism,[5,6] and catalysis.[7,8] Among these metal nanoclusters, the Au nanoclusters have been researched widely, and a few of them have been structurally characterized by single-crystal X-ray crystallography.[9−14] On the basis of the total structures of nanoclusters, a fundamental understanding of the electronic structure, optical and chiroptical, and catalytic properties has been attained.

In parallel with the thiolate-protected gold nanoclusters, significant progress has been made in the chemical synthesis of ultrasmall Ag nanoclusters protected by thiolate or coprotected by thiolate and phosphine, such as Ag_5,[15] Ag_6,[15] Ag_7,[16,17] Ag_8,[17] Ag_9,[18] Ag_{14},[19] $Ag_{14}S$,[20] Ag_{15},[21] Ag_{16},[22] Ag_{25},[23] Ag_{31},[21] Ag_{32},[22,24] Ag_{44},[25] Ag_{50},[26] Ag_{62},[27] Ag_{75},[28] Ag_{152},[29] $Ag_{70}S_{20}$,[30] $Ag_{262}S_{100}$,[30] $Ag_{320}S_{130}$,[31] and $Ag_{490}S_{188}$.[31] Moreover, their related properties have also been studied.[32,33] These studies found that some of the Ag nanoclusters have excellent luminescence properties and ultrastable nature. However, the structures of only a few of them have been successfully determined by single-crystal X-ray crystallography, such as Ag_{14},[19] Ag_{16},[22] Ag_{32},[22] Ag_{44},[25] Ag_{62},[27] Ag_{70},[30] Ag_{262},[30] Ag_{320},[31] and Ag_{490}.[31] In terms of fundamental research, the crystal structure is of major importance for achieving a better understanding of the nature of the properties. However, the total structure determination of such Ag nanoclusters by X-ray crystallography remains a major challenge.

In comparison to large nanoparticles, small-size silver/gold nanoclusters (NCs) (<3 nm) exhibit some obvious differences. Small metal nanoparticles (<3 nm) lose the bulk-like electronic properties; for example, they no longer support the plasmon excitation characteristic of relatively large nanocrystals (3−100 nm). This change makes the NCs show some major distinctions, especially in atomic packing mode and optical properties. During the past few years, face-centered-cubic (FCC) core structures in the NCs have attracted great attention due to their key roles in understanding the origin of macroscopic FCC metal materials such as gold, silver, copper, etc. Several FCC-type kernel structures have been reported thus far, including the octahedral Ag_6 kernel in $Ag_{14}(SC_6H_3F_2)_{12}(PPh_3)_8$,[19] the rodlike Au_{20} kernel in $Au_{28}(SR)_{20}$, and the tetrahedral Au_{28} kernel in $Au_{36}(SPhBu^t)_{24}$

Received: July 4, 2014
Published: October 24, 2014

   dx.doi.org/10.1021/ja506773d | J. Am. Chem. Soc. 2014, 136, 15559−15565

nanoclusters.[12,13] However, in these structures, the FCC-type structures are all incomplete, which, to a certain extent, does not allow a better understanding of the atom-packing structure of the macroscopic materials. On the other hand, complete FCC structures are prevalent for larger silver and gold nanoparticles and bulk metals. Therefore, the discovery of a metal nanocluster with a complete FCC structure is very much desired.

Herein, we report the crystal structure of $[Ag_{62}S_{12}(SBu^t)_{32}]^{2+}$ (denoted as **NC-I**). Although part of this structure is similar to that of $[Ag_{62}S_{13}(SBu^t)_{32}]^{4+}$ (denoted as **NC-II**),[27] major differences in the kernel of the structure and optical properties are observed, including the following: (1) the complete face-centered-cubic (FCC) Ag_{14} kernel is found in **NC-I**; (2) **NC-I** has four free valence electrons (i.e., 62 (silver $5s^1$) − (12 (sulfido) × 2) − 32 (thiolate) − 2 (charge) = 4), but **NC-II** has no free valence electrons; (3) in comparison with **NC-II**, the optical properties of **NC-I** show distinct differences. Moreover, femtosecond transient absorption spectroscopy has been used to identify the different changes in optical properties, and the results demonstrate that the quenching of photoluminescence is caused by the free valence electrons, which have a large effect on the ligand to metal charge transfer (LMCT) process (S 3p → Ag 5s). Moreover, we carried out TD-DFT calculations to further understand the difference between **NC-I** and **NC-II**.

2. EXPERIMENTAL SECTION

2.1. Chemicals. Silver nitrate ($AgNO_3$, 99%), glutathione (GSH, 97%), *tert*-butyl mercaptan (99%), sodium borohydride ($NaBH_4$, 99.99%), sodium tetraphenylborate ($NaBPh_4$, 99%), methanol (HPLC grade, 99%), dichloromethane (HPLC grade, 99.9%), and hexane (HPLC grade, 99.9%) were obtained from commercial sources. All chemicals were used without further purification. Pure water was obtained from Wahaha Co. Ltd. All glassware was thoroughly cleaned with aqua regia (HCl/HNO_3 3/1 v/v), rinsed with copious amounts of pure water, and then dried in an oven prior to use.

2.2. Synthesis of NC-I Nanoclusters. In a typical experiment, **NC-I** nanoclusters were synthesized by a two-phase approach, which involves two major steps: (i) the synthesis of $Ag_n(SG)_m$ clusters with a controlled size range and (ii) two-phase ligand exchange induced growth of monodisperse **NC-I** nanoclusters from the $Ag_n(SG)_m$ mixture (vide infra). The nanoclusters were crystallized from CH_2Cl_2/hexane over 2−3 days. The crystals were then collected, and the structure of **NC-I** was analyzed by X-ray crystallography.

2.2.1. Step 1: Synthesis of the $Ag_n(SG)_m$ Clusters. A mixture of $AgNO_3$ (30 mg, 0.176 mmol) and GSH (80 mg, 0.263 mmol) was dissolved in NaOH solution (50 mg of NaOH in 5 mL of water) at room temperature, and then the solution was vigorously stirred (∼1200 rpm) with a magnetic stir bar for a few minutes. A colorless solution of Ag(I)-SG complexes was obtained. After that, 5 mL of an ice-cold aqueous solution of $NaBH_4$ (20 mg) was added to the solution of the complexes. The solution gradually changed from colorless to orange and then to reddish black over a period of ∼2 min, indicating the formation of Ag:SG clusters. The reaction was allowed to proceed for 2 h.

*2.2.2. Step 2: Synthesis of **NC-I** Nanoclusters through Two-Phase Ligand Exchange.* The aqueous solution of $Ag_n(SG)_m$ was used as a precursor to prepare the final product without any purification. A 5 mL portion of dichloromethane and 2 mL of *tert*-butyl mercaptan were added. The solution was allowed to react for 10 h at room temperature with vigorous stirring. After that, the Ag clusters were completely transferred to the organic phase. During the phase transfer process, silver cluster core etching and secondary growth occurred. The isolated organic phase was dried using an evaporator, and then 3/1 (v/v) dichloromethane/methanol was added to the residual product and the solution was centrifuged at ∼6000 rpm. After removal of the precipitates, the supernatant solution was dried using an evaporator. This process was repeated until no precipitate was produced again after centrifugation. The Ag_{62} clusters as obtained were soluble in solvents such as dichloromethane and toluene. The right amount of $NaBPh_4$ was added to replace the anion, forming $[Ag_{62}S_{12}(SBu^t)_{32}]^{-}(BPh_4)_2$ for easy crystallization. The $[Ag_{62}S_{12}(SBu^t)_{32}](BPh_4)_2$ nanoclusters were crystallized in CH_2Cl_2/hexane at room temperature (2−3 days, yield 10%); dark red crystals (Figure S1b, Supporting Information) were collected and subjected to X-ray diffraction analysis to determine the structure.

2.3. X-ray Crystallographic Determination of NC-I. The data collection for single-crystal X-ray diffraction was carried out on a Bruker Smart APEX II CCD diffractometer at 173 K, using graphite-monochromated Mo Kα radiation (λ = 0.71073 Å). Data reductions and absorption corrections were performed using the SAINT and SADABS programs, respectively. The structure was solved by direct methods and refined with full-matrix least squares on F^2 using the SHELXTL software package. All non-hydrogen atoms were refined anisotropically, and all of the hydrogen atoms were set in geometrically calculated positions and refined isotropically using a riding model. Free solvent molecules were highly disordered, and location and refinement of the solvent peaks were unsuccessful. The diffuse electron densities resulting from the these residual solvent molecules were removed from the data set using the SQUEEZE routine of PLATON and refined further using the data generated. Single -crystal structural analysis revealed that **NC-I** crystallizes in a triclinic mode with the $P\bar{1}$ space group. Crystal data for **NC-I**: $C_{128}H_{288}Ag_{62}S_{44}{\cdot}2C_{24}H_{20}B$, a = 21.4604(15) Å, b = 21.6292(15) Å, c = 22.0437(17) Å, α = 88.052(2)°, β = 64.744(2)°, γ = 60.903(3)°, V = 7888.8(10) Å^3, space group $P\bar{1}$, Z =1, T = 173 K, 100384 reflections measured, 38195 unique reflections (R_{int} = 0.0263), final R1 = 0.0607 and wR2 = 0.1505 for 29737 observed reflections ($I > 2\sigma(I)$). All of the refinement parameters are summarized in Tablea S1−S3 (Supporting Information).

2.4. Transient Absorption Measurements. The femtosecond transient absorption spectra were measured at ∼90 fs time resolution using a home-built femtosecond broad-band pump−probe setup. Details of the instrument have been described elsewhere.[34,35] Briefly, a regeneratively amplified Ti:sapphire laser (Coherent Legend Elite) produced 40 fs, 1 mJ pulses at a 500 Hz repetition rate at 800 nm with a bandwidth (fwhm) of about 30 nm. The output from the amplifier was split by a 90/10 beam splitter to generate pump and probe beams. A portion of the 800 nm pulse was frequency-doubled with a 0.5 mm thick BBO (type I) crystal to provide the 400 nm pump pulse. The probe pulse at 800 nm was sent to a computer-controlled optical delay line and then focused onto a 2 mm thick water cell to generate a white light continuum which was split into two beams using a broad-band 50/50 beam splitter as the reference and signal beams. The pump power is about 100 nJ/pulse (spot size of ∼120 μm in each case) in transient absorption measurements, and no photodegradation was observed after femtosecond transient absorption measurements. To measure isotropic signals, the mutual polarizations of pump and probe beams were set to the magic angle (54.7°) using a half-wave plate. The differential absorbance $\Delta A(t,\lambda)$ was analyzed as a function of wavelength and time delay using the population dynamics modeling toolbox software developed by van Wilderen et al.[36] Spectral chirp in the transient absorption spectra was corrected for group velocity dispersion of the probe beam. Singular value decomposition (SVD) analysis was performed before the global fitting to estimate the number of components and to check for structured residuals. A sequential decay pathway was utilized to model the data $\Delta A(t,\lambda)$ which was a superposition of different spectral components $\varepsilon_l(\lambda)$ weighted by their concentration $c_l(t)$.[37]

2.5. DFT Calculations. To correlate the cluster structure and optical properties, we carried out density functional theory calculations on the electronic structures of **NC-I** and **NC-II**. The single-crystal structure derived from the XRD analysis was optimized using the Perdew−Burke−Ernzerhof (PBE) functional.[38−40] The triple-ζ polarized (TZP) basis set was adopted in all calculations using Amsterdam Density Functional (ADF 2010) software packages. The

optical absorption spectra of **NC-I** and **NC-II** were computed by the PBE functional.

2.6. Characterization. Nuclear magnetic resonance (NMR) analysis was performed on a Bruker Avance spectrometer operating at 400 MHz for ^{1}H. CD_2Cl_2 was used as the solvent to dissolve ~5 mg clusters; the residual solvent peak (i.e., ^{1}H at 5.32 ppm) was used as reference. UV−vis spectroscopic studies were carried out with an Agilent 8453 diode array spectrometer. Photoluminescence spectra were measured on a FL-4500 spectrometer.

3. RESULTS AND DISCUSSION

3.1. Crystal Structure of the NC-I Nanocluster. Single-crystal X-ray crystallography revealed that the **NC-I** nanocluster has a spherical shape containing 62 silver centers (Figure 1),

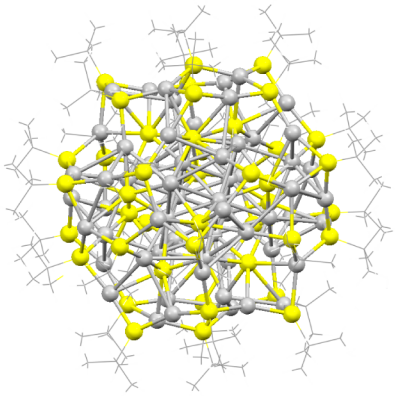

Figure 1. Crystal structure of the thiolate-protected **NC-I** nanocluster. Color labels: light gray, Ag; light yellow, S.

with two BPh_4^- groups as counterions (Figure S1a, Supporting Information), which bears similarity to the structure of $[Ag_{62}S_{13}(SBu^t)_{32}]^{4+}$ reported by Wang et al.[27] On the basis of the structure, the **NC-I** nanocluster has a Ag_6 kernel without the central S atom, which causes the **NC-I** nanocluster to become a superatom cluster, whereas the **NC-II** nanocluster is an Ag_2S quantum dot. To find out details of the atom-packing structure, below we focus on the $Ag_{62}S_{44}$ framework without the carbon tails (Figure 2a). The $Ag_{62}S_{44}$ can be divided into a complete FCC Ag_{14} kernel and an exterior $Ag_{48}(SBu^t)_{32}$ shell, which are interconnected by 12 sulfide ions.

For a more detailed anatomy of the total structure, we start with the Ag_{14} kernel (Figure 2b). The Ag_{14} kernel is presented as a complete FCC unit. In the center of the Ag_{14} kernel, there is an octahedral Ag_6, which has been reported by Zheng et al.[19] The surface of the octahedral Ag_6 kernel is enclosed by eight equilateral-triangle-shaped planes (well-defined crystal planes) (Figure 2b, green highlight), a perfect fragment that can be cut from FCC metals. Around the Ag_6 kernel, there are eight Ag atoms, which compose a perfect cube. The surface of the cubical Ag_8 is enclosed by six square shaped {100} facets (Figure 2b,c, yellow highlight). In accord with the definition of the FCC structure, we also find rectangular-shaped {110} facets (Figure 2d, blue highlight) and equilateral-triangle-shaped {111} facets (Figure 2e, pink highlight).

The distinct differences between **NC-I** and **NC-II** prompted us to recognize the Ag_{14} kernel as a single small silver cluster entity that has four nominal valence electrons of Ag 5s: i.e., Ag_{14}^{10+}. The appearance of 4e in Ag_{14}^{10+} may account for the disappearance of photoluminescence and the optical absorption difference in comparison to **NC-II**; this is due to the

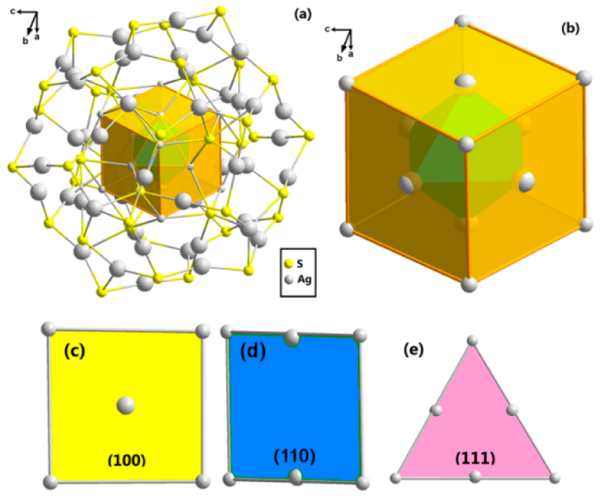

Figure 2. (a) Total structure of **NC-I**. For clariry, the connections between the Ag_{14} core and S atoms are not shown. (b) Ag_{14} core as a compete FCC unit. (c−e) Three complete crystal faces in the Ag_{14} cube.

delocalization behavior of the 4e valence electrons in **NC-I** in comparison to zero valence electron in **NC-II**. In other words, one atom (i.e., the central S atom) causes significant differences in electronic and optical properties, which is remarkable.

It is worth noting that a thiolate-protected $Ag_{14}(SC_6H_3F_2)_{12}(PPh_3)_8$ cluster was reported by Zheng et al.[19] This cluster also contains an octahedral Ag_6^{4+} unit, which is encapsulated by eight cubically arranged $[Ag^+(SC_6H_3F_2)_2PPh_3]$ tetrahedra that share one corner between them. However, the eight silver atoms in the $Ag_{14}(SC_6H_3F_2)_{12}(PPh_3)_8$ cluster did not connect with the Ag_6 core, resulting in an incomplete FCC structure of Ag_{14}; this is probably due to the presence of phosphine ligands on the cluster surface.

In the exterior shell $Ag_{48}(SBu^t)_{32}$ of **NC-I**, Ag^+ ions can be classified into two categories: 36 Ag^+ ions are at the surface, and the other 12 are located at the subsurface. All of the thiolate S atoms triply coordinate to shell silver atoms, with Ag−S bond lengths in the range 2.324(2)−2.665(2) Å, similar to the $Ag_{48}(SBu^t)_{32}$ shell of the **NC-II** nanocluster. The 12 S^{2-} ions connect the Ag_{14} kernel to the $Ag_{48}(SBu^t)_{32}$ shell through Ag_3 (kernel)−S−Ag_4 (shell).

In comparison with the structure of **NC-II** nanoclusters, the major difference lies in the Ag_6 kernel (Figure 3a,b); there is no S atom in the center of the Ag_6 kernel in the **NC-I** nanoclusters. This is seemingly a slight difference, but it causes a great impact on both the structure and electronic and optical properties as discussed above. In order to better understand the difference between the **NC-I** and **NC-II** nanoclusters, we compared the Ag_6 kernel in **NC-I** nanoclusters (denoted as **Ag_6-I**) with that in the **NC-II** nanoclusters (denoted as **Ag_6-II**) (Figure 3, highlighted in violet). In the **Ag_6-I**, the average Ag−Ag distance is 2.861 Å, which is slightly shorter than the Ag−Ag distance (ca. 2.889 Å) in bulk Ag metal. In contrast, due to the formation of the Ag−S bond, the distances of Ag−Ag (average 3.012 Å) in **Ag_6-II** are slightly longer than that of bulk Ag metal, and thus the Ag−Ag metallic-like bond cannot form (Figure 3b). The latter effect results in the failure of the formation of the octahedral Ag_6 unit (Figure 3a). As shown in Figure 3, we divide the Ag_{14} kernel into three kinds of Ag_4 planes. Without the S atoms, the distance from Ag1 (the Ag atom labeled 1) atom to plane *a* is 26.3% shorter than that in

dx.doi.org/10.1021/ja506773d | J. Am. Chem. Soc. 2014, 136, 15559−15565

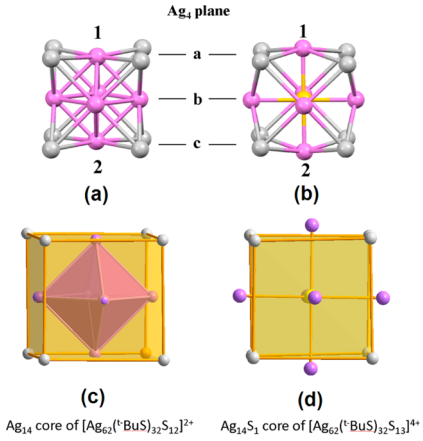

Figure 3. Structures of Ag_{14} kernels in the **NC-I** and **NC-II** nanoclusters.

the **NC-II** nanocluster; meanwhile, the distance from Ag1 to Ag2 (the Ag atom labeled 2) is 26.2% shorter than that in the **NC-II** nanocluster. These results cause the Ag_6 kernel to be wrapped in the cubic Ag_8 unit to form a complete FCC structure in the **NC-I** nanocluster (Figure 3c), which cannot be formed in the **NC-II** nanocluster (Figure 3d). Moreover, Table 1 shows some selected average bond distances, which directly

Table 1. Relevant Average Bond Distances between the Ag_{14} Kernels in NC-I and NC-II Nanoclusters As Obtained from Single-Crystal X-ray Crystallography Structures

	Ag–Ag distance (av), Å		
	NC-I	**NC-II**	diff, %
Ag(1) to pentagon a	2.994	3.001	−0.2
within plane a	4.231	4.198	+0.8
Ag(1) to pentagon b	2.861	3.614	**−26.3**
within plane b	2.855	3.610	**−26.4**
between a and b	3.022	3.017	+0.2
Ag(2) to pentagon b	2.861	3.614	**−26.3**
between b and c	3.022	3.017	+0.2
within plane c	4.231	4.198	+0.8
Ag(1) to Ag (2)	4.056	5.118	**−26.2**
Ag(1) to bridging Ag atom	3.171	2.718	+14.3

show the difference between **NC-I** and **NC-II**. These differences not only change the location of Ag atoms but also convert the Ag–S type Ag_6 unit into a superatom type Ag_6 kernel, which induces the distribution of the 4e valence electrons.

In order to confirm the formula of **NC-I**, we performed a nuclear magnetic resonance (NMR) analysis. In the ^{1}H NMR spectrum of **NC-I** (Figure 4a), the peaks at 6.75–7.50 ppm (40 H) are assigned to $-C_6H_5$ in Ph_4B^- and the peaks at 1.65–1.80 ppm (288 H) are assigned to $-CH_3$ in the $-SBu^t$ ligands. According to the proton ratio (C_6H_5:CH_3 = 40:288), we determined that the ratio of $[Ag_{62}S_{12}(SBu^t)_{32}]^+$ to Ph_4B^- is 1:2. This indicates that the precise formula of **NC-I** is $[Ag_{62}S_{12}(SBu^t)_{32}](BPh_4)_2$, which is consistent with the X-ray crystallographic analysis.

Moreover, due to the similar exterior shells between **NC-I** and **NC-II**, we also divide the thiolate ligands into two types (Figure 4b): type A is coordinated to three silver atoms at the surface, and type B is ligated to two silver atoms at the surface

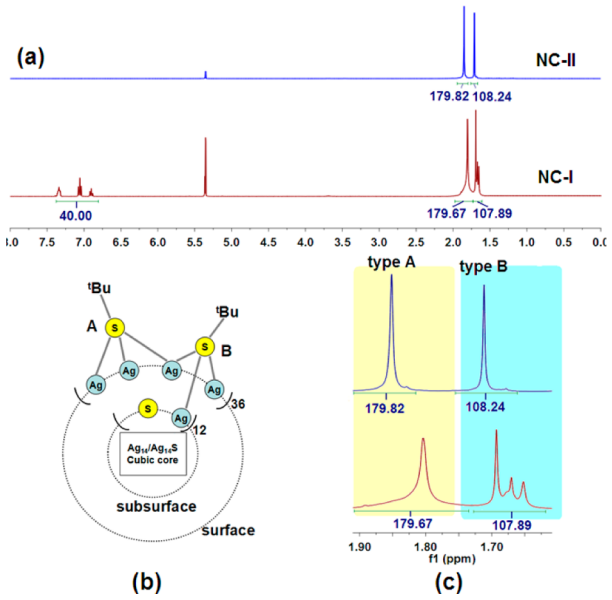

Figure 4. (a) ^{1}H NMR spectra of **NC-I** and **NC-II**. (b) Two types of bonding environments of $-SBu^t$ ligands in **NC-I** and **NC-II**. (c) Enlarged view of the ^{1}H NMR spectra (single crystal dissolved in CD_2Cl_2).

and one silver atom at the subsurface. In order to better analyze the difference between **NC-I** and **NC-II**, the ^{1}H NMR spectrum of **NC-II** was also measured (Figure 4a) and a zoom-in of the peaks at 1.60–2.00 ppm is provided (Figure 4c). As shown in Figure 4c, **NC-II** in CD_2Cl_2 showed two resonances (1.91 and 1.71 ppm) in a ratio of 5:3, which is consistent with the numbers of the two types of ^{t}BuS– ligands (type A (20) vs type B (12)), which is consistent with a previous report (the minor shift is caused by the solution effect).[27] With the four free valence electrons, the peaks of type A in **NC-I** shift to 1.80 ppm, and the resonances of type B in **NC-I** shift to 1.69 ppm with two small peaks (1.65 and 1.67 ppm). The proton ratio of types A and B is 180:108, indicating that the composition of the obtained crystals is homogeneous. To further confirm this, we picked 15 pieces of single crystals at random and got identical UV–vis spectra, which show absorption bands at 420 and 520 nm (Figure 5a, red line). We have carried out electrospray ionization mass spectrometry (ESI-MS) of the **NC-I** (Figure S2, Supporting Information). Similar to the case for **NC-II**,[27] the intact ion peak also cannot be observed, which is due to the large exterior shell $(Ag_{48}(SBu^t)_{32})$.

Furthermore, recent works suggest that there are two forms in the silver clusters. One is a superatom cluster such as the $Ag_{44}(SR)_{30}$ nanocluster,[25] which has a composition of $[Ag_{12}@Ag_{32}(SR)_{30}]^{4-}$. The other is an Ag_2S quantum dot like nanocluster: for example, an **NC-II** nanocluster that has a composition of $\{(Ag_2S)_{13}[Ag_{36}(SBu^t)_{32}]\}^{4+}$.[27] The superatom clusters possess a certain number of free valence electrons and thus exhibit conductivity and superconductivity properties, while the other form of Ag clusters can be treated as a typical semiconductor.[41,42] Any intermediate-phase structure, which contains the characteristics of the superatom nanoclusters and quantum dot nanoclusters, would be a very interesting structure that could potentially contribute to an understanding of the nature of nanoclusters. The **NC-I** nanocluster contains a FCC

dx.doi.org/10.1021/ja506773d | J. Am. Chem. Soc. 2014, 136, 15559–15565

Ag_{14} kernel and a Ag_2S quantum dot shell, which fits the structure described above.

3.2. Optical Properties of NC-I and NC-II. In addition to the difference between the structures of **NC-I** and **NC-II**, **NC-I** also exhibits prominent differences in the optical properties in comparison with those of the **NC-II** nanocluster. First, the optical absorption spectrum of **NC-I** nanoclusters (dissolved in CH_2Cl_2) shows two stepwise peaks at 420 and 520 nm (Figure 5a), whereas the optical spectrum of **NC-II** (dissolved in CH_2Cl_2) shows peaks at 330, 370, and 543 nm.[27] Second, the **NC-II** nanocluster emits red photoluminescence under ambient light or 365 nm excitation,[27] while there is almost no fluorescence from the **NC-I** nanocluster (Figure 5b; note the 900× scaling up).

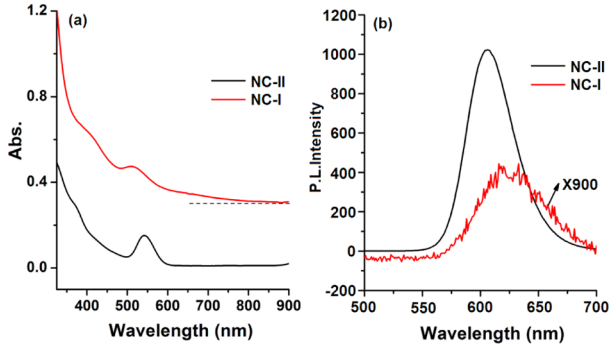

Figure 5. (a) UV−vis absorption spectra and (b) photoluminescence spectra of **NC-I** and **NC-II**.

In order to further study the differences, broad-band transient absorption (pump−probe) measurements with excitation at 400 nm were performed to investigate the excited-state processes. Both excited-state absorption (ESA, positive signal) and ground-state bleaching (GSB, negative signal) were observed in the two NCs (Figure 6). For **NC-II**, ESA peaks appeared at 500 and 590 nm overlapped with GSB at 540 nm. In the first 10 ps, the ESA at 590 nm decayed to give rise to the ESA at 500 nm (see the inset of Figure 6a), suggesting the formation of an intermediate state. After global fitting, we extracted a fast spectral component with a lifetime of 0.8 ps and another long-lived component (>1 ns). The population dynamics show that the rise and decay of the two spectral components follow the sequential model during the relaxation (see Figure 6b). Since the emission of **NC-II** has been assigned to the S 3p to Ag 5s charge transfer (ligand to metal charge transfer, LMCT),[27] the long-lived ESA at 500 nm could originate from the LMCT state. The efficient quenching of the ESA at 500 nm after dissolution of O_2 further confirms the assignment of this transient absorption to the triplet LMCT state (see Figure S3 in the Supporting Information). Thus, these two spectral components can be ascribed to the metal core state and LMCT state within the **NC-II** cluster, respectively. In comparison with **NC-II**, completely different spectral properties were observed for **NC-I**. The ESA at 560 nm has no obvious decay within the initial several picoseconds. The global fit gives two spectral components with time constants of 3.5 and 800 ps (Figure 6d). Unlike that in **NC-II**, the ESA at 500 nm is absent for the long-lived component, suggesting that the LMCT state is not formed in **NC-I**. On the basis of previous ultrafast investigation in Au NCs,[34,43,44] **NC-I** can be assigned to the core state (3.5 ps) and surface state (800 ps) at the interface of metal/ligands, respectively. In any event, according to the spectral shape from the obtained species associated difference spectra (SADS) and kinetics, it is more likely that the relaxations result from the vibration relaxation (3.5 ps) of the excited ICT state after 400 nm excitation and then decay to the ground state from the relaxed ICT state with a time constant of about 800 ps. The distinct differences between **NC-I** and **NC-II** prompted us to recognize the central

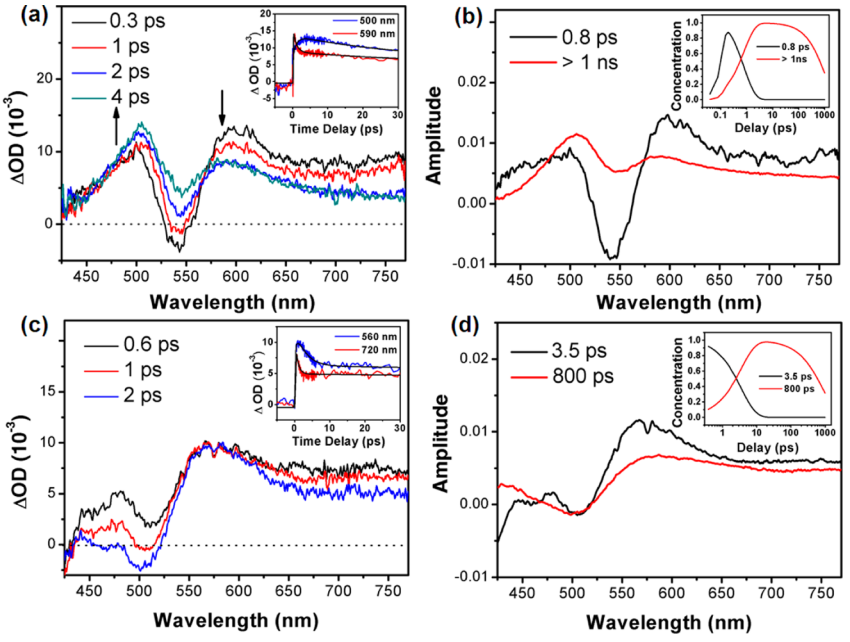

Figure 6. Evolution-associated transient absorption spectra at different time delays (a, c) and species associated difference spectra (SADS) obtained from singular value decomposition (SVD) combined with global fitting (b, d) for solutions of the NCs **NC-II** (a, b) and **NC-I** (c, d). The insets in (a, c) show the fitted kinetics at specific wavelengths, and the insets in (b, d) show the population dynamics of each component obtained from global fitting results, respectively.

dx.doi.org/10.1021/ja506773d | J. Am. Chem. Soc. 2014, 136, 15559−15565

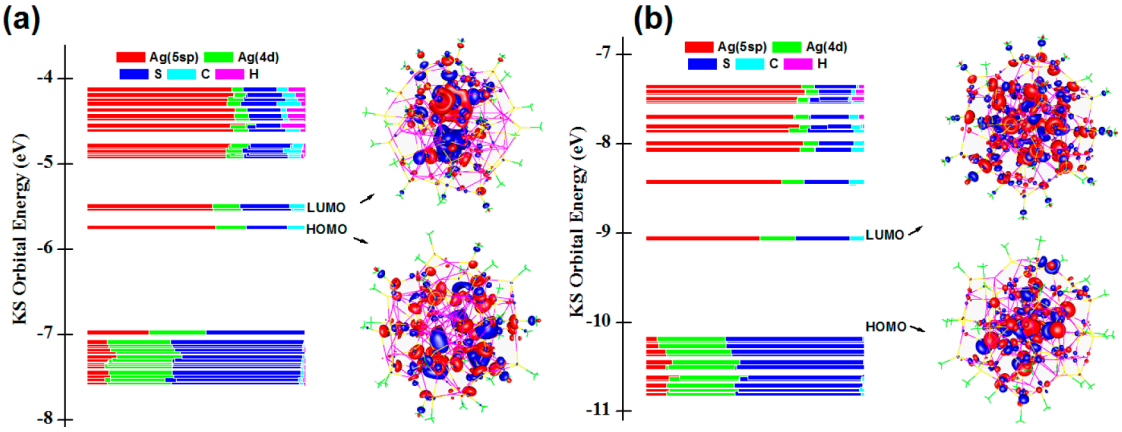

Figure 7. Kohn–Sham (KS) molecular orbital energies and the associated populations of atomic orbitals in each KS molecular orbital for (a) **NC-I** and (b) **NC-II**. The electron densities of the highest occupied molecular orbital (HOMO) and the lowest unoccupied molecular orbital (LUMO) are displayed for both clusters.

kernel (Ag_{14}/$Ag_{14}S$) as a single small silver cluster. In **NC-II**, all of the Ag atoms do not have nominal valence electrons of Ag 5s, i.e. $(SAg_{14})^{12+}$, leading to the formation of a triplet LMCT state with fluorescence emission, whereas **NC-I** has four nominal valence electrons of Ag 5s: i.e., Ag_{14}^{10+}. The appearance of 4e in Ag_{14}^{10+} may account for the disappearance of photoluminescence and the optical absorption difference in comparison to **NC-II**; this is due to the delocalization behavior of the 4e valence electrons in **NC-I** in comparison to zero valence electron in **NC-II**, which prevents the charge transfer from the ligands to the metal core; thus, the formation of the triplet LMCT state is inhibited during the relaxation. In other words, the electronic structure causes significant differences in electron dynamics and optical properties.

3.3. TD-DFT Analysis of the Electronic Structures of the NC-I and NC-II Clusters. DFT calculations were further performed to investigate the electronic structures of **NC-I** and **NC-II** clusters. The major striking difference between the electronic structures of **NC-II** and **NC-I** is that the former cluster has the electron density concentrated on the inner $Ag_{14}S_{13}$ kernel in HOMO and the LUMO has the electron density mostly distributed at the outer AgS shell of the cluster. A reverse electron density distribution is found in **NC-I** (Figure 7a). The LUMO of **NC-I** has the electron density localized mostly on the $Ag_{14}S_{12}$ kernel. The theoretical analysis suggests that, during the electron excitation, the electron transition between the HOMO and the LUMO in the two clusters has different manners. In **NC-II** (Figure 7b), the HOMO → LUMO transition involves the electron migration from the $Ag_{14}S_{13}$ kernel to the outer AgS shell. However, the electron migration from the outer AgS shell to the Ag_{14} core is expected during the HOMO → LUMO transition in **NC-I**.

A significant decrease in HOMO–LUMO gap is found from **NC-II** to **NC-I**. The **NC-II** has a HOMO–LUMO gap much larger than that of **NC-I** (Figure 7). A more careful examination of energy levels of KS orbitals indicates that a sizable energy gap exists between the HOMO and HOMO-1 of **NC-I**, which suggests that the further removal of two electrons from **NC-I** may lead to an increased HOMO–LUMO gap in the cluster. We computed the optical absorption of **NC-I** and **NC-II** by using the PBE functional (Figure S4, Supporting Information). However, the calculated spectra have a large red shift in comparison to the experimental results. Improvement of the computational methods on such complicated silver nanoclusters needs further research.

4. CONCLUSION

The crystal structure of the $[Ag_{62}S_{12}(SBu^t)_{32}]^{2+}$ nanocluster has been successfully determined. In comparison with the reported $[Ag_{62}S_{13}(SBu^t)_{32}]^{4+}$ NCs, the free valence electrons (4e for **NC-I**) have been found. With the existence of the valence electrons and the absence of a center S atom, the middle Ag_{14} core largely shrinks, and this results in the formation of a complete FCC unit in $[Ag_{62}S_{12}(SBu^t)_{32}]^{2+}$ NCs. Meanwhile, the existence of free valence electrons changes the optical properties of the NCs, especially in the quenching of photoluminescence. The femtosecond transient absorption spectra suggest that the quenching of photoluminescence is caused by the free valence electrons in the $[Ag_{62}S_{12}(SBu^t)_{32}]^{2+}$ nanocluster, because such electrons largely change the ligand to metal charge transition (LMCT, S 3p → Ag 5s). These findings offer new insight into the structure and property evolution of silver cluster materials.

■ ASSOCIATED CONTENT

Supporting Information

Figures, tables, and a CIF files giving detailed information about the digital photo of **NC-I**, ESI-MS spectrum, evolution-associated transient absorption spectra, calculated optical absorption spectra, and X-ray analysis of $[Ag_{62}S_{12}(SBu^t)_{32}](BPh_4)_2$. This material is available free of charge via the Internet at http://pubs.acs.org.

■ AUTHOR INFORMATION

Corresponding Author

*E-mail for M.Z.: zmz@ahu.edu.cn.

Author Contributions

‖These authors contributed equally to this work.

Notes

The authors declare no competing financial interest.

■ ACKNOWLEDGMENTS

We acknowledge financial support by the NSFC (21072001, 21201005, 21372006), the Ministry of Education and Ministry of Human Resources and Social Security, the Education Department of Anhui Province, the Anhui Province Interna-

tional Scientific and Technological Cooperation Project, and the 211 Project of Anhui University.

REFERENCES

(1) Rosi, N.; Giljohann, D.; Thaxton, C.; Lytton-Jean, A.; Han, M.; Mirkin, C. *Science* **2006**, *312*, 1027.
(2) Wohltjen, H.; Snow, A. *Anal. Chem.* **1998**, *70*, 2856.
(3) Huang, C.; Chiang, C.; Lin, Z.; Lee, K.; Chang, H. *Anal. Chem.* **2008**, *80*, 1497.
(4) Lin, C.; Yang, T.; Lee, C.; Huang, S.; Sperling, R.; Zanella, M.; Li, J.; Shen, J.; Wang, H.; Yeh, H.; Parak, W.; Chang, W. *ACS Nano* **2009**, *3*, 395.
(5) Zhu, M.; Aikens, C.; Hendrich, M.; Gupta, R.; Qian, H.; Schatz, G.; Jin, R. *J. Am. Chem. Soc.* **2009**, *131*, 2490.
(6) Antonello, S.; Perera, N.; Ruzzi, M.; Gascón, J.; Maran, F. *J. Am. Chem. Soc.* **2013**, *135*, 15585.
(7) Chong, H.; Li, P.; Wang, S.; Fu, F.; Xiang, J.; Zhu, M.; Li, Y. *Sci. Rep.* **2013**, *3*, 3214.
(8) Li, G.; Zeng, C.; Jin, R. *J. Am. Chem. Soc.* **2014**, *136*, 3673.
(9) Das, A.; Li, T.; Nobusada, K.; Zeng, C.; Rosi, N.; Jin, R. *J. Am. Chem. Soc.* **2013**, *135*, 18264.
(10) Jadzinsky, P.; Calero, G.; Ackerson, C.; Bushnell, D.; Kornberg, R. *Science* **2007**, *318*, 430.
(11) Heaven, M.; Dass, A.; White, P.; Holt, K.; Murray, R. *J. Am. Chem. Soc.* **2008**, *130*, 3754.
(12) Zeng, C.; Li, T.; Das, A.; Rosi, N.; Jin, R. *J. Am. Chem. Soc.* **2013**, *135*, 10011.
(13) Zeng, C.; Qian, H.; Li, T.; Li, G.; Rosi, N.; Yoon, B.; Barnett, R.; Whetten, R.; Landman, U.; Jin, R. *Angew. Chem., Int. Ed.* **2012**, *51*, 13114.
(14) Qian, H.; Eckenhoff, W.; Zhu, Y.; Pintauer, T.; Jin, R. *J. Am. Chem. Soc.* **2010**, *132*, 8280.
(15) González, B.; Blanco, M.; López-Quintela, M. *Nanoscale* **2012**, *4*, 7632.
(16) Wu, Z.; Lanni, E.; Chen, W.; Bier, M. E.; Ly, D.; Jin, R. *J. Am. Chem. Soc.* **2009**, *131*, 16672.
(17) Rao, T.; Pradeep, T. *Angew. Chem., Int. Ed.* **2010**, *49*, 3925.
(18) Rao, T.; Nataraju, B.; Pradeep, T. *J. Am. Chem. Soc.* **2010**, *132*, 16304.
(19) Yang, H.; Lei, J.; Wu, B.; Wang, Y.; Zhou, M.; Xia, A.; Zheng, L.; Zheng, N. *Chem. Commun.* **2013**, *49*, 300.
(20) Jin, X.; Tang, K.; Liu, W.; Zeng, H.; Zhao, H.; Ouyang, Y.; Tang, Y. *Polyhedron* **1996**, *15*, 1207.
(21) Bertorelle, F.; Hamouda, R.; Rayane, D.; Broyer, M.; Antoine, R.; Dugourd, P.; Gell, L.; Kulesza, A.; Mitric, R.; Bonacic-Koutecky, V. *Nanoscale* **2013**, *5*, 5637.
(22) Yang, H.; Wang, Yu.; Zheng, N. *Nanoscale* **2013**, *5*, 2674.
(23) Remya, K.; Udayabhaskararao, T.; Pradeep, T. *J. Phys. Chem. C* **2012**, *116*, 26019.
(24) Guo, J.; Kumar, S.; Bolan, M.; Desireddy, A.; Bigioni, T.; Griffith, W. P. *Anal. Chem.* **2012**, *84*, 5304.
(25) (a) Harkness, K.; Tang, Y.; Dass, A.; Pan, J.; Kothalawala, N.; Reddy, V.; Cliffel, D.; Demeler, B.; Stellacci, F.; Bakr, O. *Nanoscale* **2012**, *4*, 4269. (b) Desireddy, A.; Conn, B.; Guo, J.; Yoon, B.; Barnett, R.; Monahan, B.; Kirschbaum, K.; Griffith, W.; Whetten, R.; Landman, U.; Bigioni, T. *Nature* **2013**, *501*, 399. (c) Yang, H.; Wang, Y.; Huang, H.; Gell, L.; Lehtovaara, L.; Malola, S.; Häkkinen, H.; Zheng, N. *Nat. Commun.* **2013**, *4*, 2422. (d) AbdulHalim, L.; Ashraf, S.; Katsiev, K.; Kirmani, A.; Kothalawala, N.; Anjum, D.; Abbas, S.; Amassian, A.; Stellacci, F.; Dass, A.; Hussain, I.; Bakr, O. *J. Mater. Chem. A* **2013**, *1*, 10148. (e) Chakraborty, I.; Kurashige, W.; Kanehira, K.; Gell, L.; Hakkinen, H.; Negishi, Y.; Pradeep, T. *J. Phys. Chem. Lett.* **2013**, *4*, 33.
(26) Tang, K.; Xie, X.; Zhang, Y.; Zhao, X.; Jin, X. *Chem. Commun.* **2002**, 1024.
(27) Li, G.; Lei, Z.; Wang, Q. *J. Am. Chem. Soc.* **2010**, *132*, 17678.
(28) Chakraborty, I.; Udayabhaskararao, T.; Pradeep, T. *Chem. Commun.* **2012**, *48*, 6788.
(29) Chakraborty, I.; Govindarajan, A.; Erusappan, J.; Ghosh, A.; Pradeep, T.; Yoon, B.; Whetten, R.; Landman, U. *Nano Lett.* **2012**, *12*, 5861.
(30) Fenske, D.; Persau, C.; Dehnen, S.; Anson, C. *Angew. Chem., Int. Ed.* **2004**, *43*, 305.
(31) Anson, C.; Eichhofer, A.; Issac, I.; Fenske, D.; Fuhr, O.; Sevillano, P.; Persau, C.; Stalke, D.; Zhang, J. *Angew. Chem., Int. Ed.* **2008**, *47*, 1326.
(32) Chen, M.; Dyer, J.; Li, K.; Dixon, D. *J. Phys. Chem. A* **2013**, *117*, 8298.
(33) Gell, L.; Kulesza, A.; Petersen, J.; Rohr, M.; Mitrić, R.; Bonacić-Koutecky, V. *J. Phys. Chem. C* **2013**, *117*, 14824.
(34) Zhou, M.; Vdović, S.; Long, S.; Zhu, M.; Yan, L.; Wang, Y.; Niu, Y.; Wang, X.; Guo, Q.; Jin, R.; Xia, A. *J. Phys. Chem. A* **2013**, *117*, 10294.
(35) Zhou, M.; Long, S.; Wan, X.; Li, Y.; Niu, Y.; Guo, Q.; Wang, Q.; Xia, A. *Phys. Chem. Chem. Phys.* **2014**, *16*, 18288.
(36) van Wilderen, L.; Lincoln, C.; van Thor, J. *PLoS One* **2011**, *6*, e17373.
(37) van Stokkum, H.; Larsen, D.; van Grondelle, R. *Biochim. Biophys. Acta* **2004**, *1657*, 82.
(38) Perdew, J.; Burke, K.; Ernzerhof, M. *Phys. Rev. Lett.* **1996**, *77*, 3865.
(39) Aikens, C. *J. Phys. Chem. A* **2009**, *113*, 10811.
(40) Pei, Y.; Lin, S.; Su, J.; Liu, C. *J. Am. Chem. Soc.* **2013**, *135*, 18067.
(41) Schnçckel, H. *Chem. Rev.* **2010**, *110*, 4125.
(42) Schnepf, A. *Chem. Soc. Rev.* **2007**, *36*, 745.
(43) Du, Y.; Xu, B.; Fu, T.; Cai, M.; Li, F.; Zhang, Y.; Wang, Q. *J. Am. Chem. Soc.* **2010**, *132*, 1470.
(44) Devadas, M.; Kim, J.; Sinn, E.; Lee, D.; Goodson, T.; Ramakrishna, G. *J. Phys. Chem. C* **2010**, *114*, 22417.